Unified modeling of cellular responses to diverse perturbation types

Chen Li[1], Lei Wei[1*] and Xuegong Zhang[1,2*]

1 MOE Key Laboratory of Bioinformatics and Bioinformatics Division of BNRIST, Department of Automation, Tsinghua University, Beijing 100084, China

2 Center for Synthetic and Systems Biology, School of Life Sciences and School of Medicine, Tsinghua University, Beijing 100084, China

* To whom correspondence should be addressed. Email: zhangxg@tsinghua.edu.cn; weilei92@tsinghua.edu.cn

Abstract

Predicting cellular responses to perturbations is essential for understanding gene regulation and advancing drug development. Most existing *in silico* perturbation models treat perturbation–cell interactions with simplistic fusion strategies that overlook the hierarchical nature of regulatory processes, leading to inaccurate predictions and poor generalization across perturbation types. We present X-Pert, a universal *in silico* perturbation model that explicitly captures both gene–perturbation interactions and gene–gene dependencies through attention mechanisms. X-Pert flexibly handles diverse perturbation inputs across different types and combinations, and quantitatively models their dosage- and efficacy-dependent effects, all within a unified representation space. This enables accurate prediction of unseen, combinatorial, and dose- or efficacy-dependent responses of various perturbation types. Across benchmarks spanning genetic and chemical perturbations, X-Pert consistently demonstrates superior performance at both gene and pathway levels. Moreover, its unified representation space enables downstream analyses such as perturbation retrieval and drug–gene association discovery. By integrating data across perturbation types, experimental platforms, and cell contexts, X-Pert establishes a versatile and generalizable foundation for *in silico* perturbation, enabling broad applications in biological and therapeutic discovery.

Introduction

In silico perturbation aims to predict gene expression changes induced by genetic[1-7], chemical[8-12], or protein-based[13-16] interventions, expanding our ability to explore perturbation outcomes at scale and supporting mechanistic discovery, cellular engineering, and drug development. A variety of computational methods have been developed for *in silico* perturbation[17-30], including models based on graph neural networks (GNNs)[17, 18], variational autoencoders (VAEs)[22-24], and transformers[19, 20]. While these approaches aim to capture global expression responses, they fail to reflect how perturbations propagate through hierarchical regulatory cascades that progressively reshape global expression programs and cell states. Most existing models approximate this complex process with simple embedding operations, such as concatenating or adding perturbation and cell representations, to predict transcriptional responses. This oversimplification neglects the context-dependent interaction between perturbations and cell states and overlooks the hierarchical nature of gene regulation, ultimately leading to inaccurate predictions, weak generalization, and limited interpretability.

These limitations not only hinder accurate modeling of intracellular regulatory processes but also restrict the applicability of current methods when extended to broader perturbation types. Most existing *in silico* perturbation methods are designed for a specific perturbation type, such as either genetic or chemical interventions. Although a few approaches[28, 29] have been explored across multiple perturbation types, they generally require training separate models for each dataset rather than learning within a shared representation space. With the rapid expansion of heterogeneous perturbation datasets, this separate training strategy has become a major bottleneck, as it fails to reflect the biological reality that different classes of perturbations often converge on shared regulatory mechanisms to reshape gene expression and cell states. Learning these shared mechanisms in a unified way is therefore critical for achieving cross-perturbation generalization and deeper mechanistic interpretability. A unified framework that can accommodate diverse perturbation types within a single representation space is thus essential for capturing shared principles of cellular responses and enabling more accurate response prediction.

To address these challenges, we propose X-Pert, a unified framework for modeling cellular responses to diverse perturbation types. X-Pert adopts a transformer backbone with latent query tokens that represent different external perturbations in a shared representation space, enabling joint training across both genetic and chemical perturbation datasets as well as extending naturally to additional perturbation types such as cytokine perturbations[31]. Through a combination of cross-attention and self-attention mechanisms, X-Pert explicitly captures gene–perturbation and gene–gene interactions, thereby modeling the hierarchical regulatory processes that determine how perturbations reshape transcriptional programs. We benchmark X-Pert across both genetic and chemical perturbation tasks, using not only conventional metrics that measure prediction accuracy across the entire expression profile but also new biology-aware metrics that assess the prediction on top differentially expressed genes and pathway-level responses. Across these comprehensive benchmarks, X-Pert consistently outperforms existing methods, achieving higher predictive accuracy and

capturing biologically meaningful variation among perturbations. Moreover, perturbations of varying dosage, combination, and type can be consistently embedded into a unified latent space, supporting downstream applications including perturbation retrieval, drug–gene association discovery, combinatorial perturbation prediction, and dose- or efficacy-aware prediction. Together, these capabilities position X-Pert as a versatile and generalizable framework that bridges genetic mechanisms and pharmacological interventions, offering a systematic foundation for understanding and designing cellular perturbations.

Results

X-Pert: a unified model for *in silico* perturbation

We designed X-Pert to predict the gene expression profile of a perturbed cell from the original cell and the corresponding perturbation information. Unlike previous approaches that treat different perturbation types separately, X-Pert integrates perturbation signals and cellular context within a unified architecture to capture their fine-grained interactions.

The model consists of two key components: the Perturbation Perceiver and the Cell Encoder (Fig. 1, Methods). The Perturbation Perceiver maps perturbations of different types into a shared latent representation space. Each perturbation type is first initialized as a fixed-length embedding by a type-specific encoder (in this work, we used text embeddings from GPT-4o[32] for genetic perturbations, and SMILES-based embeddings computed with RDKit[33] for chemical perturbations). Dose or perturbation efficacy information, when available, is then incorporated by augmenting the corresponding perturbation embedding. Depending on the experimental setting, a single perturbation embedding or a set of embeddings for multiple perturbations is then passed through a Perceiver Resampler, where a fixed set of learnable latent query tokens are employed to transform these embeddings into unified perturbation tokens (Methods). These tokens define a shared representation space that enables unified characterization of perturbations and their combinations, which we term the Perturbverse.

The unified perturbation tokens produced by the Perturbation Perceiver serve as conditional context for the Cell Encoder, a transformer-based module designed to predict perturbed gene expression profiles by modeling both gene–perturbation interactions and gene–gene dependencies (Methods). The Cell Encoder builds upon a large cellular model to encode an original cell as a sequence of gene identity tokens and expression value tokens (Methods). To better incorporate perturbation effects, we introduce an Impact Tokenizer that encodes perturbation-specific influences on each gene. The formulation of impact tokens is designed to flexibly accommodate different perturbation types: for genetic perturbations, they are modeled as one-hot vectors marking perturbed genes; for chemical perturbations, they are derived from protein–molecule affinity scores predicted by a pre-trained drug–target binding affinity prediction model[34] (Methods). Each gene token is then summarized by integrating its gene identity, expression value, and impact components. These summarized

gene tokens interact with perturbation tokens through cross-attention to capture perturbation–gene relationships. Subsequently, self-attention layers are employed to model gene–gene dependencies and preserve the intrinsic regulatory structure of the cell. The Cell Encoder outputs normalized gene expression values for the perturbed cell.

X-Pert is trained end-to-end with a mean squared error (MSE) loss between predicted and observed profiles (Methods). Once trained, it serves not only as a robust predictor of cellular responses but also as a versatile framework for downstream biological discovery. The Perturbverse serves as a unified reference space that enable cross-perturbation analysis, supporting perturbation retrieval and gene–drug association discovery. The Cell Encoder flexibly handles diverse datasets and biological contexts, supporting the prediction of single or multiple perturbations as well as dose- or efficacy-dependent responses. These capabilities establish X-Pert as both a powerful *in silico* perturbation predictor and a general foundation for applications in biology and medicine.

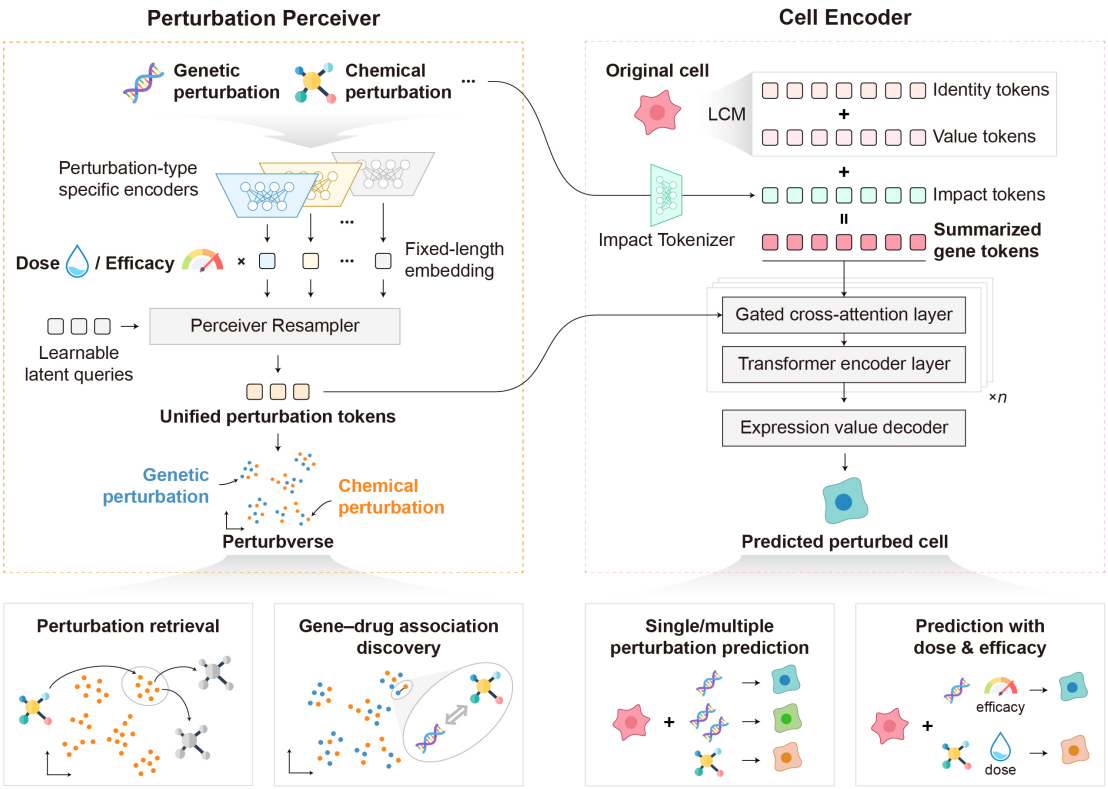

Fig. 1. Overview of the model architecture of X-Pert. X-Pert consists of two core components: the Perturbation Perceiver and the Cell Encoder. The Perturbation Perceiver is designed to accommodate different types of external perturbations, including multiple simultaneous perturbations and dose- or efficacy-dependent effects. Through a set of learnable latent queries, it projects perturbations of any type and number into a fixed-length latent representation, termed the Perturbverse. The Cell Encoder models the original cell using three types of tokens, namely identity tokens, value tokens, and impact tokens, which respectively encode gene identity, expression magnitude, and perturbation influence. By combining a gated cross-attention module with transformer encoder layers, the Cell Encoder integrates perturbation information with original gene expression to predict the transcriptional profile of perturbed cells. X-Pert can be applied to

a wide range of perturbation-based tasks. Leveraging the Perturbverse, X-Pert enables perturbation retrieval and gene–drug association discovery through similarity analysis. Using the Cell Encoder's predictive capability, X-Pert supports single/combinatorial perturbation prediction as well as modeling of perturbation efficacy and dose–response relationships.

Predicting responses of unseen genetic perturbations

We first evaluated X-Pert's performance on unseen genetic perturbation prediction, representing a real-world use case in which the model infers cellular responses to perturbations not yet experimentally profiled within the same cell type (Fig. 2A). To evaluate this capability, we benchmarked X-Pert on three single-cell perturbation datasets spanning CRISPR interference[4] (CRISPRi, Replogle2022_K562 and Replogle2022_RPE1) and CRISPR activation[35] (CRISPRa, Norman2019), comprising between 224 and 1,299 unique perturbations (Methods). For each dataset, perturbations were split 8:2 into training and testing (Methods). We compared X-Pert with six representative methods, including linear models[36] (Linear, Linear-scGPT), deep learning methods (CellOracle[37], GEARS[17]), and large cellular foundation models (scGPT[20], scFoundation[19]), and the mean predictor (AveKnown) that have been used as a naive baseline in some studies[28, 38].

We first evaluated model performance using a commonly used metric, the Pearson correlation coefficient (PCC) across all genes, referred to as PCC_All, which quantifies the correlation between predicted and observed gene-expression changes for each perturbation, calculated over all genes as paired values of predicted and measured expression differences relative to the original cells. As shown in Fig. 2B, X-Pert achieved the best or highly competitive performance on PCC_All across all three datasets. However, we found that PCC_All provides little meaningful differentiation among models, as even naïve predictors such as AveKnown perform similarly. A recent study has revealed a pervasive systematic bias in genetic-perturbation datasets, where shared global response components dominate gene-expression variance, overshadowing the true perturbation-specific regulatory signals[39]. Consequently, even simple baselines such as AveKnown can achieve deceptively high correlation scores by reproducing these shared patterns, a phenomenon consistently reported across benchmarks[36, 38]. Therefore, while PCC_All remains a convenient and widely used summary statistic, it primarily reflects the recovery of background structure rather than the accurate modeling of biological perturbation effects.

To better assess biological relevance responses, we next examined PCC_DEG, which quantifies the correlation between predicted and observed expression changes only among DEGs (Methods). This metric filters out nonspecific or noisy variation and provides a clearer view of biologically meaningful transcriptional responses. For instance, it reached 0.720 on Replogle2022_K562, a 13.2% improvement over the second-best method, with similar gains observed on Replogle2022_RPE1 (+3.8%). Importantly, most methods showed a larger increase in performance when evaluated by PCC_DEG compared with PCC_All across datasets. This

consistent widening of the performance gap suggests that PCC_DEG captures perturbation effects more faithfully by highlighting genuine expression changes associated with each perturbation, which are largely averaged out in PCC_All by shared global responses. However, despite this improvement, the PCC_DEG of AveKnown remains high, indicating that this metric still carries dataset-level correlations and is limited in distinguishing biologically meaningful variation from background effects. These limitations underscore the need for evaluation strategies that move beyond correlation-based similarity and instead assess a model's ability to reconstruct both the magnitude and the functional organization of true perturbation effects.

To move beyond correlation-based metrics and directly assess how accurately each model captures real perturbation effects, we focused on perturbations with at least 20 significant DEGs. This subset reflects conditions where transcriptional regulation is strongly altered and thus provides a clearer test of biological fidelity. For each perturbation, we compared the predicted and observed expression changes of the top 20 DEGs, which represent the most strongly responsive genes and are typically related to the downstream functional consequences of the perturbation. This evaluation highlights not only whether a model predicts the correct direction of change but also whether it reproduces the actual magnitude of transcriptional shifts. For example, in the POLA1 perturbation of Replogle2022_K562, X-Pert closely recapitulated both the direction of magnitude of top 20 DEGs' expression changes, whereas other methods tended to compress predictions toward low-magnitude shifts (Fig. 2C). Similar patterns were observed for additional perturbations across datasets (Fig. S1A). We further quantified this agreement using the coefficient of determination (R^2) between the predicted and observed expression changes of the top DEGs (Methods). Across all three datasets, X-Pert consistently achieved the highest R^2 scores (Fig. 2D and Fig. S1B), demonstrating its ability to accurately reproduce the real magnitudes of perturbation-induced transcriptional responses rather than merely capturing overall expression trends.

While single-gene evaluations help assess whether a model can reproduce individual expression changes, cellular responses are in fact mediated by coordinated regulation of gene programs. Therefore, evaluating predictions at the pathway level provides a more biologically meaningful and noise-robust assessment of model performance. To assess pathway-level responses, we computed Hallmark gene set scores[40] for each perturbation by averaging the corresponding signature scores across all cells under that condition (Methods), reflecting the activation state of specific pathways after perturbation. Such evaluation moves beyond conventional correlation-based metrics, as it directly tests whether a model can recover the coordinated activation or repression of biological programs that define a cell's functional state. We quantified the agreement between predicted and observed gene set scores across different perturbations using PCC (PCC_GS). Unlike gene-level metrics that assess agreement within each perturbation, PCC_GS compares model performance across perturbations, evaluating whether the model can correctly rank perturbations by the magnitude and direction of their pathway-level effects. This distinction is important because the ability to prioritize perturbations by their functional impact forms the basis for many biological applications such as perturbation retrieval, target identification, and mechanism inference.

On 260 test perturbations from the Replogle2022_K562 dataset, X-Pert captured this diversity with high fidelity. For example, in the DNA repair gene set, it achieved the highest PCC_GS (0.40), representing a 53.8% improvement over the second-best method, GEARS (PCC_GS = 0.26, Fig. 2E). In contrast, AveKnown completely failed under this setting, producing identical predictions for all perturbations and thus showing no ability to distinguish functional differences between them. Furthermore, X-Pert successfully predicted a cluster of perturbations exhibiting coordinated decreases in DNA repair gene set scores within the UMAP space, a structure that none of the other methods were able to capture (Fig. 2E). Similar advantages were observed for additional gene sets such as adipogenesis, apical junction, and protein secretion (Fig. S1C). Across all 50 Hallmark gene sets, X-Pert consistently outperformed all other methods (Fig. 2F), demonstrating superior ability to model perturbation-specific gene program changes.

These results demonstrate that X-Pert not only achieves accurate performance across multiple evaluation metrics but also provides biologically coherent predictions at both gene and pathway levels. These findings also highlight that pathway-level benchmarks, by comparing relative perturbation effects across perturbations rather than isolated gene-level predictions within a single perturbation, provide a more faithful measure of biological realism. Such benchmarks align with findings from a recent perturbation benchmark[39] that emphasized evaluating performance across the full spectrum of perturbations rather than isolated cases.

Building on X-Pert's strong predictive performance, we next examined what the model has learned about the underlying structure of perturbations. We explored the interpretability of X-Pert's learned latent perturbation space, or Perturbverse, generated by the Perturbation Perceiver (Methods). Because perturbations are represented using gene-related text embeddings, even perturbations absent from training can be directly embedded into the space (Fig. 2G). This provides a structured representation of perturbation effects for revealing functional relationships among genetic perturbations. For instance, 504 genetic perturbations from Replogle2022_K562 revealed clusters corresponding to biological processes such as proteasome, mediator complex, and DNA replication, despite only 209 perturbations being included in training (Fig. 2H and S2A).

The Perturbverse also provides a convenient framework to examine how clusters of perturbation genes relate to downstream expression changes. By mapping all input perturbations into the Perturbverse (Methods), we found that proteasome-related perturbations formed a coherent cluster, and their predicted profiles showed coordinated upregulation of multiple subunits (PSMB5, PSMD1, PSMD13), consistent with the known "bounce-back" transcriptional response[41, 42] (Fig. 2H–I). A similar Perturbverse constructed for Replogle2022_RPE1, despite being trained on only 73 perturbations, also recovered clear and biologically coherent structures (Fig. S2A–B). These results highlight that X-Pert not only achieves accurate prediction of unseen genetic perturbations but also organizes them into an interpretable latent space that reveals functional relationships between perturbation clusters and transcriptional programs.

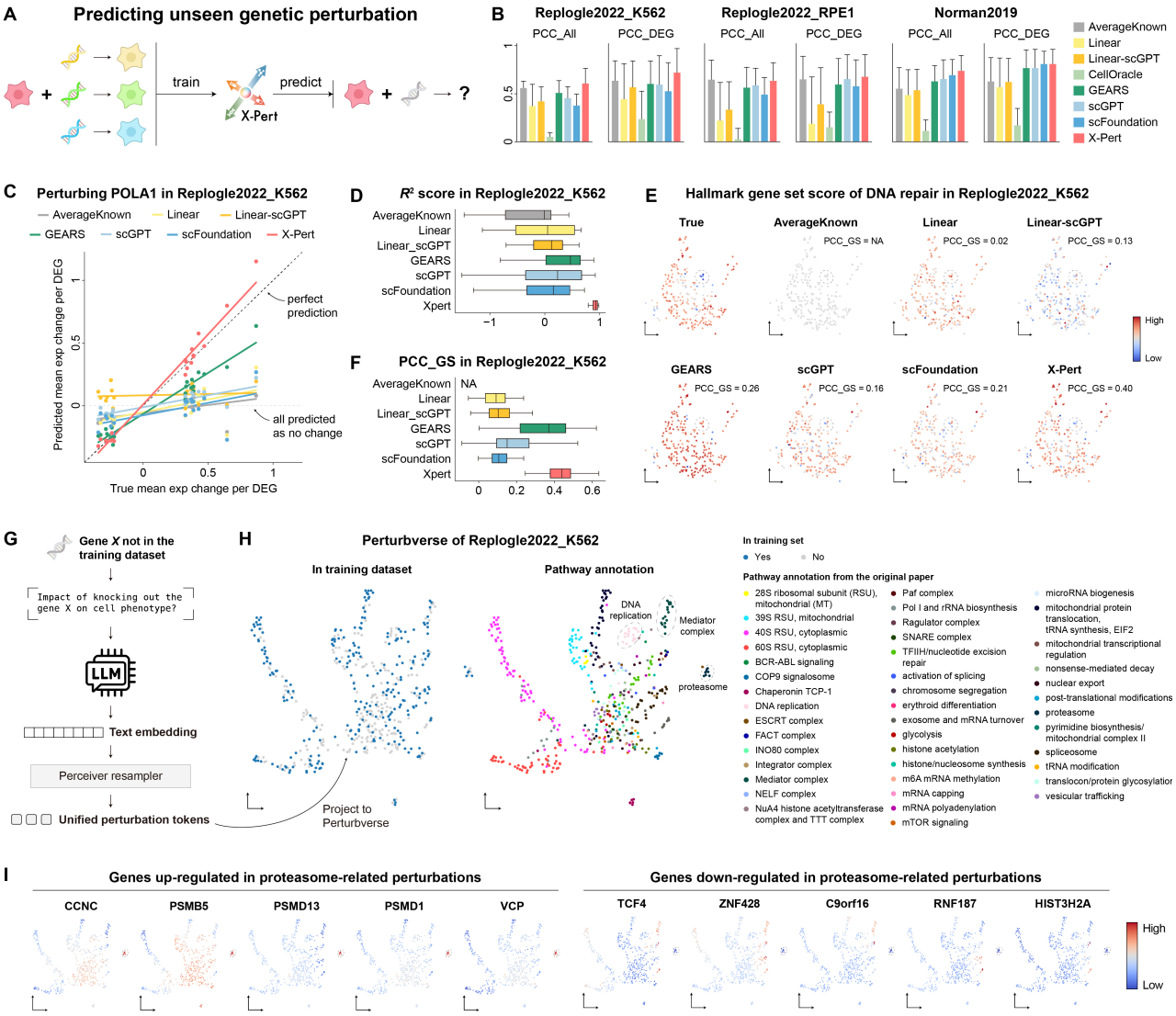

Fig. 2. X-Pert's predictions of genetic perturbations. (A) Schematic illustration of predictions on unseen genetic perturbations. **(B)** Comparison of X-Pert with other methods. **(C)** Comparison between predicted and ground-truth expression changes of the top 20 DEGs following POLA1 perturbation in Replogle2022_K562. Dots represent the mean predicted expression changes from each method, and a linear regression fit was added to visualize the correlation between the predicted and true mean values. CellOracle is not included because it only performs prediction on transcription factors. **(D)** Box plots comparing the R^2 score between predicted and observed expression changes of top 20 DEGs in Replogle2022_K562. **(E)** UMAP visualization of Hallmark DNA repair gene set scores. The leftmost panel shows ground-truth scores, and each point represents a genetic perturbation. The PCC_GS between predicted and observed gene set scores is shown in each panel. The dashed circle highlights the ground-truth clustering of perturbations with reduced gene set scores. **(F)** Box plots comparing the PCC_GS of all 50 Hallmark gene sets across 260 test perturbations in Replogle2022_K562. For bar plots, bar: mean performance value; error bar: standard deviation across replicates. For box plots, center line, median; box limits, upper and lower quartiles; whiskers, 1.5× interquartile range. **(G)** Schematic illustration of using latent tokens from the Perturbverse to explore the functional landscape of genetic perturbations. **(H)** UMAP visualization of 504 genetic perturbations from Replogle2022_K562, with pathway annotations manually curated from the original dataset. **(I)** UMAP visualization of mean gene expressions across

504 annotated genetic perturbations from Replogle2022_K562. The ten displayed genes were selected from significant DEGs in proteasome-related perturbations. Dashed circles represent cells perturbed by proteasome-related genes.

Predicting responses under perturbation combinations and considering efficacy

The flexible design of the Perturbation Perceiver enables X-Pert to naturally handle both combinatorial perturbations and perturbation efficacy. To assess its ability to generalize to unseen combinations (Fig. 3A), we used the Norman2019 dataset, which includes 148 single-gene and 76 two-gene CRISPRa perturbations. To simulate the unseen-combination setting, we randomly excluded 30% of the single-gene perturbations during training and evaluated two types of double perturbations: one-unseen combinations (n = 61), where one perturbed gene was absent from training, and two-unseen combinations (n = 15), where both were unseen. Notably, the evaluation did not include "zero-unseen" combinations, as such cases do not naturally arise from this data-splitting strategy.

As shown in Fig. 3B, X-Pert substantially outperformed all other methods in the one-unseen setting across all metrics. Even in the more challenging two-unseen setting, X-Pert maintained the best performance in in R^2 score and PCC_GS, and remained highly competitive in PCC_All and PCC_DEG. Notably, X-Pert was the only model that achieved a clearly positive median PCC_GS in the two-unseen setting, underscoring its capacity to generalize to novel perturbations by leveraging gene-related text embeddings for perturbation representation. Together, these results demonstrate that X-Pert effectively integrates multiple perturbations and extends robustly to unseen combinatorial conditions.

Modeling perturbation efficacy represents another important challenge (Fig. 3C). For example, In CRISPR-based experiments, perturbation efficacy depends heavily on sgRNA design but is not directly measurable, unlike chemical perturbations where dose provides a natural quantitative proxy. To address this, we quantified genetic perturbation efficacy by measuring target gene downregulation relative to original cells (Methods), and examined its relationship with the overall transcriptional impact, quantified by the energy distance (E-distance) between perturbed and original profiles. For the full Replogle2022_K562 dataset, we didn't find global correlation between E-distance and perturbation efficacy (Fig. 3D). This is likely because many perturbations induce weak or noisy transcriptional shifts, which obscure the link between efficacy and downstream effects. However, focusing on a more homogeneous subset of 37 ribosomal protein large subunit (RPL) perturbations, we observed a significant negative correlation (PCC = –0.43, p = 0.0085; Fig. 3D), indicating that higher efficacy generally drives stronger transcriptional responses. These findings suggest that efficacy information should be explicitly incorporated into predictive models.

Building on this insight, we extended X-Pert to incorporate efficacy information, yielding X-Pert_efficacy (Methods). Across all perturbations in Replogle2022_K562, X-Pert_efficacy performed comparably to or

slightly better than the original model (Fig. 3E). When investigating the RPL subset, it showed a clear advantage: X-Pert_efficacy achieved significantly higher R^2 on eight held-out perturbations (Fig. 3E) and more faithfully recovered expression changes of top DE genes (Fig. 3F and Fig. S3). For example, in the case of RPL14 perturbation, it can more accurately predicted expression changes in top DEGs, which were underestimated by the original model (Fig. 3F). Similar improvements were consistently observed across other test RPL perturbations (Fig. S3), highlighting the value of incorporating efficacy information into the predictive framework.

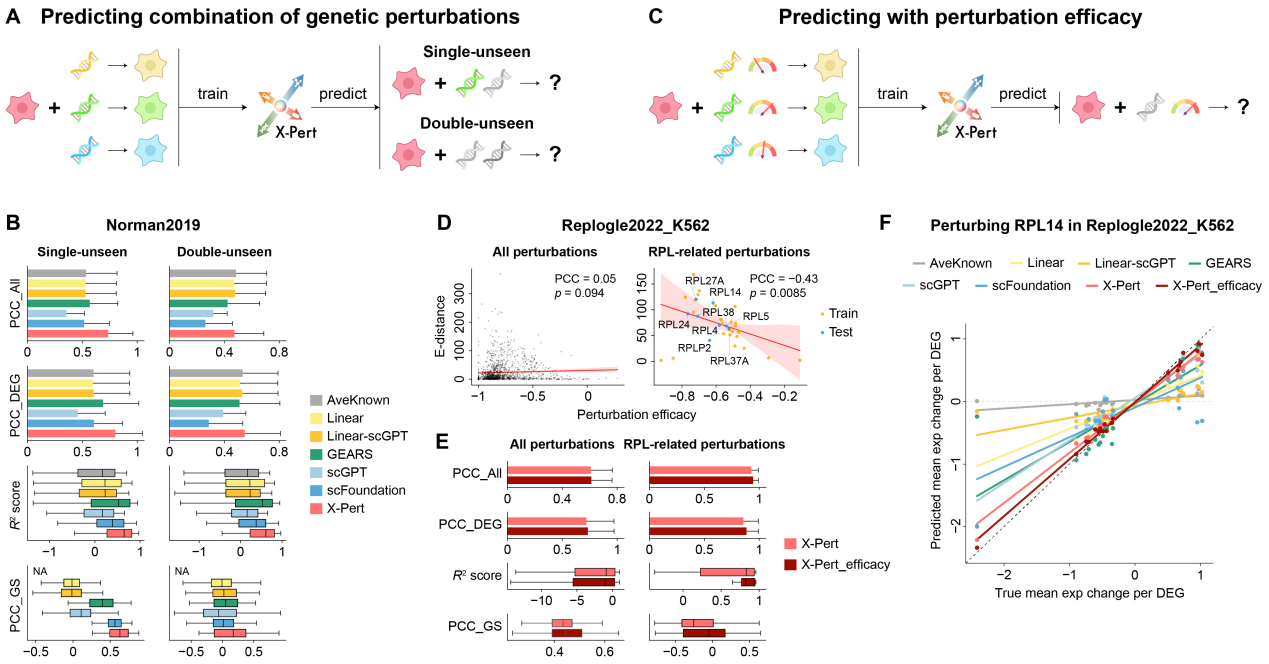

Fig. 3. X-Pert's predictions of perturbation combinations and with efficacy modeling. (A) Schematic illustration of multi-perturbation prediction. **(B)** Comparison of X-Pert with other methods in the combinatorial perturbation prediction setting. For bar plots, bar: mean performance value; error bar: standard deviation across replicates. For box plots, center line, median; box limits, upper and lower quartiles; whiskers, 1.5× interquartile range. **(C)** Schematic illustration of perturbation prediction incorporating efficacy information. **(D)** Scatter plots with fitted regression lines showing the relationship between E-distance and perturbation efficacy across all perturbations (left) and RPL-related perturbations (right) in Replogle2022_K562. **(E)** Bar plots comparing X-Pert and X-Pert_efficacy across all test perturbations (left) and RPL-related perturbations (right). **(F)** Comparison between predicted and ground-truth expression changes of the top 20 DEGs following RPL14 perturbation in Replogle2022_K562. Dots represent the mean predicted expression changes from each method, and a linear regression fit was added to visualize the correlation between the predicted and true mean values.

Predicting responses of chemical perturbations

We next evaluated X-Pert on chemical perturbations (Fig. 4A), We first benchmarked it on the Sciplex-3 dataset[11], which profiles three cell lines (A549, K562, MCF7) treated with 188 drugs across four

concentrations (10 nM–10,000 nM, 758,368 cells after preprocessing). Perturbations were split 8:2 into training and testing. We selected representative chemical perturbation prediction methods for comparison, including ChemCPA[24], BioLord[25], and PRnet[26]. As shown in Fig. 4B, X-Pert achieved the best or highly competitive performance across PCC_All, PCC_DEG, and R^2 score, and reached the highest PCC_GS in K562 and MCF7. However, the overall predictive performance across all models was modest, with median R^2 scores close to zero. This limitation appears to arise from the intrinsic characteristics of the Sciplex-3 dataset: most perturbations induced only a small number of significant DEGs, even with higher compound concentrations (Fig. S4A). Such weak transcriptional responses result in a low signal-to-noise ratio, making it difficult for models to learn robust perturbation-response relationships.

To test whether X-Pert captures dose-dependent effects, we examined the M344 perturbation in MCF7 cells as a case study. M344 is a histone deacetylase (HDAC) inhibitor with marked dose-dependent heterogeneity, currently under investigation for its therapeutic potential in cancer and Alzheimer's disease[43]. Across the top 10 DEGs, X-Pert faithfully reproduced dose–response patterns, capturing both trends and magnitudes of change (Fig. 4C). Similar results were observed across other compounds (Fig. S4B), confirming the effectiveness of explicit dose modeling.

We further extended the evaluation to the CMAP (Connectivity Map) dataset[44], a large bulk-level perturbation resource profiling 17,775 small molecules across 70 cell lines using the L1000 technology (678,401 profiles after preprocessing). The diversity of CMAP allows testing on unseen molecules and unseen cell types, posing greater challenges than single-cell datasets. To account for bulk-level measurements, we evaluated both PCC_All and R^2 (PCC_DEG and PCC_GS were excluded from the evaluation because the L1000 technology already selected 978 genes for profiling; R^2 was calculated based on all profiled genes). As shown in Fig. 4D, X-Pert consistently outperformed all other methods under both settings. On unseen molecules, it exceeded BioLord by 3.1% in PCC_All and 12.0% in R^2. On unseen cell types, the gains were even larger (PCC_All +11.4%, R^2 +74.3%), underscoring X-Pert's ability to capture drug responses in diverse cellular contexts.

We then explored whether chemical perturbations form meaningful representations in the Perturbverse. For 851 CMAP molecules with DrugBank ATC level 1 annotations[45], original embeddings lacked discernible organization, whereas X-Pert grouped molecules into functionally coherent clusters, such as "antineoplastic and immunomodulating agents" (Fig. 4E and Fig. S4C). This enrichment is biologically reasonable, as nearly all CMAP profiles were generated from cancer-derived cell lines, likely leading X-Pert to amplify signals from antineoplastic drugs.

Finally, we tested the utility of X-Pert for drug retrieval (Fig. 4F) by projecting ~30,000 natural compounds from the natural compound database HERB 2.0[46] into the Perturbverse and ranking them by cosine similarity to reference antineoplastic drugs (Fig. 4G, Methods). Among the top 20 retrieved candidates, nearly half have documented anticancer activity (Fig. 4H), including diterpenoid quinones[47] (e.g., Agastaquinone), taxane-type

diterpenoids[48, 49] (Taxezopidines K and G), and caffeoylquinic acid derivatives[50, 51] (3-O-caffeoyl-4-O-sinapoylquinic acid), all consistent with known pharmacological properties. In addition, structurally related analogues of paclitaxel (e.g., N-debenzoyl-N-cinnamoyltaxol) emerged, suggesting potential therapeutic relevance.

Together, these results demonstrate that X-Pert not only predicts chemical perturbation responses with high accuracy, including dose-dependent effects, but also organizes perturbations into biologically meaningful embeddings that enable *in silico* drug retrieval and discovery.

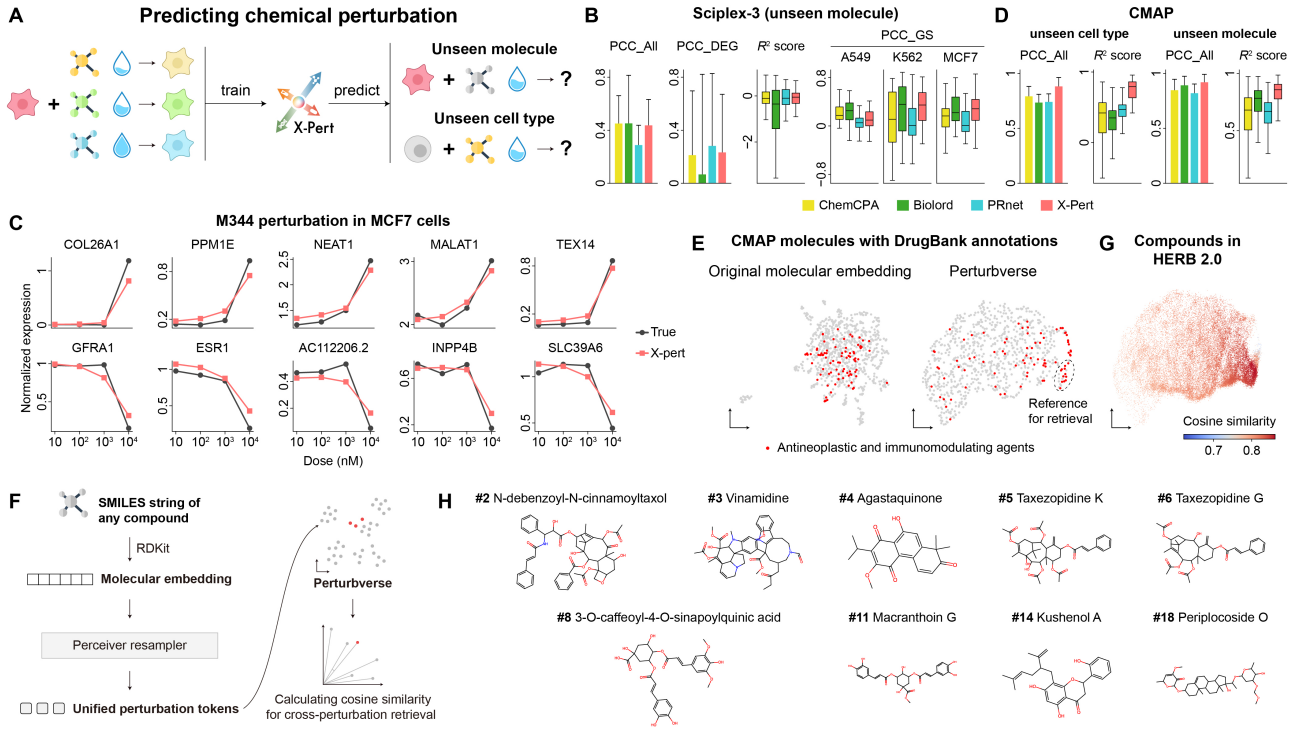

Fig. 4. X-Pert predictions on chemical perturbations. (A) Schematic illustration of chemical perturbation prediction. **(B)** Model comparison on the Sciplex-3 dataset under the unseen molecule prediction scenario. **(C)** Line plots showing X-Pert–predicted gene expression levels versus ground-truth measurements across four chemical doses. **(D)** Model comparison on the CMAP dataset under both unseen molecule and unseen cell type settings. **(E)** UMAP visualization of chemical perturbations in the original molecular embedding space and the Perturbverse, colored by ATC Level 1 annotations. **(F)** Schematic illustration of the drug retrieval process using latent chemical embeddings derived from the Perturbverse. **(G)** UMAP visualization showing the cosine similarity distribution of candidate molecules from the HERB 2.0 database. **(H)** Top-ranked molecules retrieved by X-Pert from the HERB 2.0 database, shown with their rankings and compound names. For bar plots, bar: mean performance value; error bar: standard deviation across replicates. For box plots, center line, median; box limits, upper and lower quartiles; whiskers, 1.5× interquartile range.

In silico drug screening using large-scale chemical perturbation data

To extend X-Pert to *in silico* drug screening, we trained it on Tahoe-100M[12], the largest publicly available

single-cell chemical perturbation dataset to date. Generated with the Mosaic platform, Tahoe-100M comprises ~100 million cells across 379 compounds, each profiled at three doses in 50 cell lines. This breadth of compounds and contexts makes it an ideal resource for large-scale perturbation modeling. To improve computational efficiency, we aggregated single-cell profiles into pseudo-bulk measurements (Methods), which preserved perturbation signals while enabling tractable training. Perturbations were split 8:2 into training and testing.

X-Pert accurately reconstructed the transcriptomic distributions of different cell lines in the UMAP space, clearly distinguishing them from one another (Fig. 5A), indicating that X-Pert not only predicts gene expression but also captures cell line-specific contexts. However, closer inspection of A549 cells revealed that plate labels introduced a strong batch effect, which masked drug-specific signals (Fig. 5B). To mitigate this, we incorporated a linear regression-based adjustment to remove batch-associated variation before drug screening (Methods). After correction, we implemented an *in silico* drug screening pipeline (Fig. 5C, Methods): for each disease, we curated up- and down-regulated gene sets as disease signatures, computed gene set scores under candidate perturbations (denoted as up-scores and down-scores), and identified drugs with lower up-scores and higher down-scores with more potential that could reverse disease signatures. This strategy allowed drug ranking to reflect genuine therapeutic potential rather than technical noise.

We applied this approach to prioritize drugs for three cancer types: pancreatic ductal adenocarcinoma (PDAC; Panc 03.27), hepatocellular carcinoma (HCC; HepG2), and lung adenocarcinoma (LUAD; NCI-H1792). From an FDA-approved drug list, we excluded compounds used for training, yielding 831 candidates. X-Pert ranked the top ten drugs for each cancer.

As shown in Fig. 5D, for PDAC, top candidates included glucocorticoids (desonide, meprednisone, and dexamethasone acetate), which have shown unexpected anti-tumor activity in PDAC models[52]. X-Pert also highlighted Pracinostat, a pan-HDAC inhibitor under clinical investigation[53]. Another strong candidate was Entospletinib, a selective SYK inhibitor originally developed for B-cell cancers[54], with evidence of reshaping tumor immunity[55] and overcoming PDAC chemoresistance[56], as supported by related compounds in preclinical models. For HCC, X-Pert identified nitroxoline, a cathepsin B inhibitor with well-documented anti-liver cancer effects[57]. Another candidate, clioquinol, an 8-hydroxyquinoline derivative, exerts anticancer activity through metal chelation, proteasome inhibition, and apoptosis induction[58], and preclinical studies reported its antiproliferative effects in liver cancer cells[59]. Empagliflozin, an SGLT2 inhibitor approved for diabetes[60] with emerging evidence of benefit in preclinical HCC models[61], was also prioritized. For LUAD, X-Pert prioritized sotagliflozin, consistent with the reliance of LUAD on SGLT2-mediated glucose uptake[62] and clinical signals of benefit from SGLT2 inhibitors in NSCLC patients[63]. It also highlighted ciclopirox, which suppresses proliferation and induces apoptosis in LUAD models[64], and veliparib, a PARP inhibitor with reported benefit in NSCLC subgroups[65].

Together, these results show that X-Pert can integrate large perturbation datasets with disease-specific

transcriptional signatures to prioritize candidate drugs across different cancer types, demonstrating its potential as a practical tool for accelerating drug discovery and repurposing.

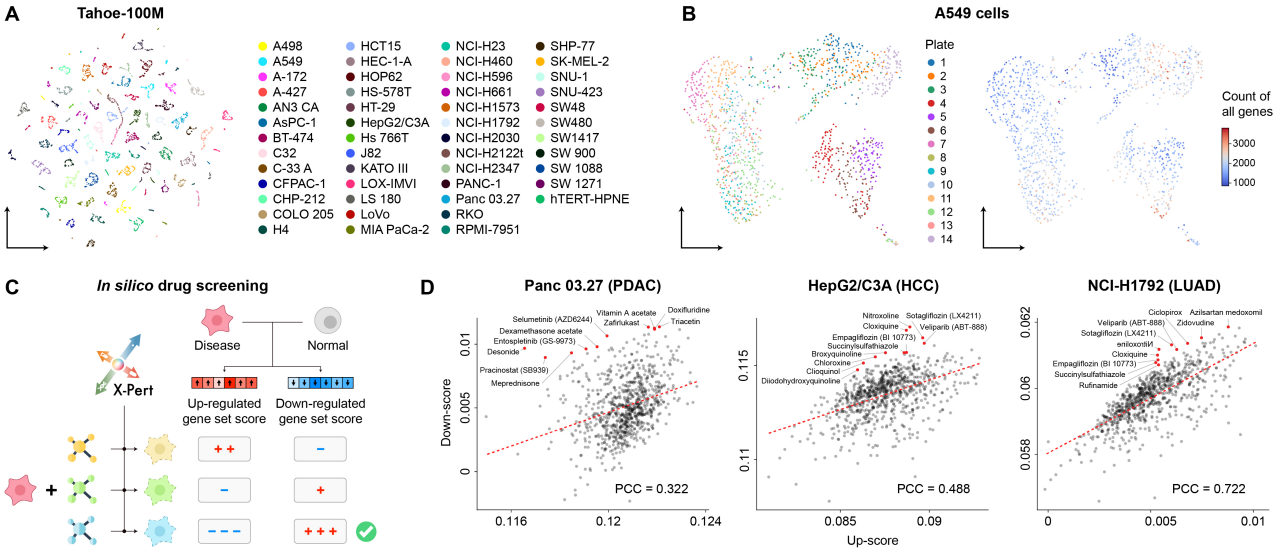

Fig. 5. *In silico* drug screening using the Tahoe-100M dataset. (A) UMAP visualization of test perturbations predicted by X-Pert, where each point represents a pseudo-bulk cell derived from a specific chemical perturbation in a cell line. Points are colored by cell line. **(B)** UMAP visualization of all A549 samples, colored by sequencing plate and count of all genes, respectively, highlighting potential batch effects. **(C)** Schematic illustration of the *in silico* drug screening pipeline. **(D)** Scatter plots showing the top-ranked candidate drugs and fitted regression lines for three diseases: PDAC, HCC, and LUAD. Lower up-scores and higher down-scores represent drugs with higher potential that could reverse disease signatures. The top ten prioritized drugs are annotated in red.

Aligning genetic and chemical perturbations in Perturbverse

The unified design of the Perturbation Perceiver allows X-Pert to jointly model multiple perturbation types within a unified framework. To evaluate this capability, we used the CMAP dataset, which contains both genetic and chemical perturbations profiled on same cell lines. We focused on three cell lines with the largest number of dual–perturbation-type profiles: A549 (21,685 chemical and 3,620 genetic perturbations), VCAP (34,753 chemical, 3,641 genetic), and HT29 (14,513 chemical, 3,302 genetic), and trained X-Pert independently on each cell line with an additional Maximum Mean Discrepancy (MMD) loss to encourage cross-type alignment (Methods).

We first quantitatively evaluated X-Pert's ability to align genetic and chemical perturbations. Visualization of the Perturbverse showed that genetic and chemical perturbations were well integrated (Fig. 6A). We selected a set of representative genes, including AKT1, AKT2, CTSK, SMAD3, TP53, MTOR, BRAF, and PIK3CA, as they represent diverse, therapeutically relevant signaling pathways and are associated with known or putative small-molecule modulators. For each gene, we queried GDIdb[66] to identify drugs interacting with

it, yielding 7–23 compounds per gene. We then calculated the cosine similarity between the latent embeddings of these drugs and their corresponding genes learned by X-Pert. As shown in Fig. 6B, ground-truth gene–drug pairs consistently showed higher cosine similarity than random drug–gene pairs for most genes across all three cell lines. These results confirm that X-Pert effectively captures functional correspondence between genetic and chemical perturbations.

To assess its generalization, we focused on the HT29 cell line and examined the test perturbations that were excluded from model training (Fig. 6C). The low-dimensional visualization revealed that genetic and chemical perturbations were also well fused. Subgroups in this space revealed biologically plausible relationships. For example, in subgroup 1, deltaline aligned with NAIP deletion, both reducing muscle contraction despite distinct mechanisms[67, 68]; tetramethylpyrazine hydrochloride (TMPH) aligned with MAP2K4 knockout, both suppressing JNK signaling[69, 70]. Other examples included vicriviroc aligning with VIM knockdown, both of which impair tumor cell invasion[71, 72], and farnesylthioacetic acid aligning with RASGRP4 knockdown, both suppressing Ras-dependent signal transduction and thus reducing proliferation and promoting apoptosis[73, 74]. Subgroup 2 showed parallels such as aliskiren with MRGPRD loss, both protecting cardiovascular cell function by attenuating angiotensin II (Ang II) signaling[75, 76]. Likewise, MRGPRD knockout showed functional similarity to anti-inflammatory drugs such as clocortolone pivalate and limonin[77-79]. Besides, both PTPRG loss and alpha-linolenic acid supplementation improved insulin sensitivity and reduced inflammation[80, 81]. Together, these results highlight X-Pert's capacity to align genetic and chemical perturbations in a unified latent space and to uncover biologically meaningful relationships between perturbations.

We further evaluated X-Pert's ability to perform cross-type perturbation retrieval within the Perturbverse of HT29 cells. HT29, a human colon cancer cell line harboring the BRAF V600E mutation, is frequently used to study the effectiveness of targeted therapies that inhibit the BRAF–MEK–ERK signaling pathway[82]. We queried the BRAF perturbation embedding of Perturbverse against 1,919 natural compounds from the Selleckchem database[83], and we found a distinct subset of compounds with exceptionally high similarity scores to the BRAF perturbation embedding (Fig. 6D). We then identified top 10 candidates with high similarity (Fig. 6E). The top-one candidate is Astragaloside A, which, though not a direct enzymatic inhibitor of BRAF, have been shown to modulate the MAPK/ERK pathway[84], thereby producing functional outcomes comparable to inhibition of RAF/MEK signaling. Another prominent group, including glycyrrhizic acid and its derivatives (including ammonium glycyrrhizinate and diammonium glycyrrhizinate), has been shown to act as RAS allosteric inhibitors[85]. We also identified Fargesin which has been reported to inhibit the PKA/CREB and p38 MAPK pathways, thereby affecting cellular processes regulated by the MAPK family[86]. While its mechanism does not directly target BRAF, its modulation of MAPK downstream kinases, such as ERK and p38[87], suggests potential functional convergence with BRAF inhibition.

Taken together, these results demonstrate that X-Pert's latent space can not only align genetic and chemical

perturbations but also retrieve compounds that mimic the effects of gene depletion. This highlights the model's potential as a framework for flexible drug discovery and repurposing.

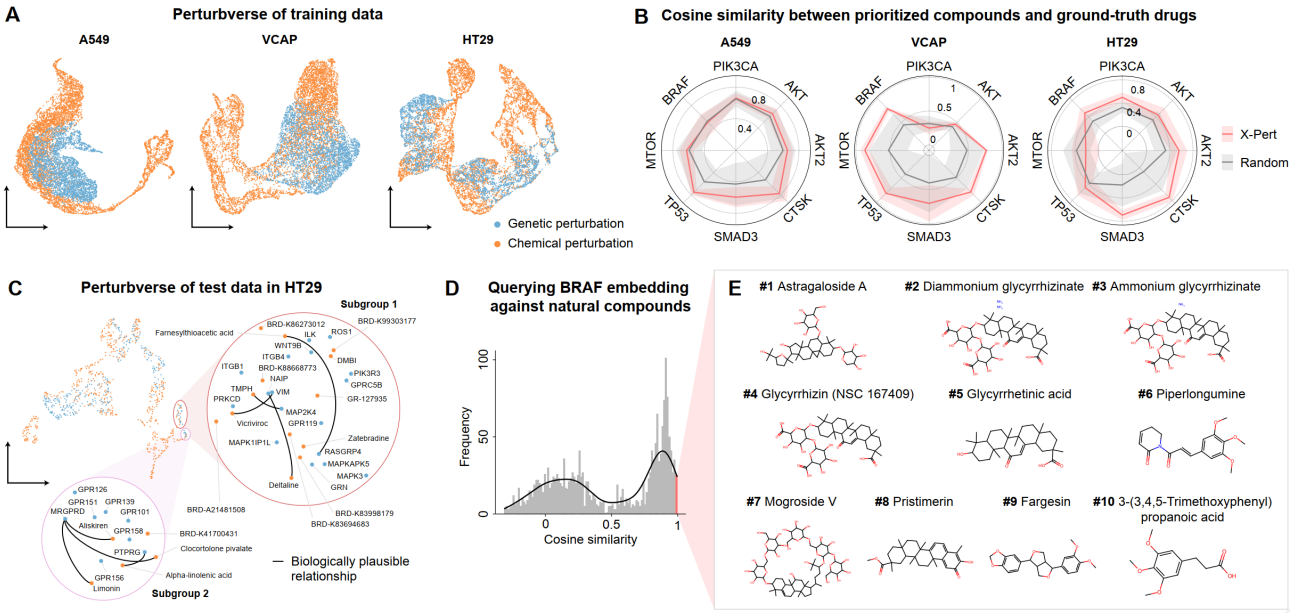

Fig. 6. Cross-type alignment with genetic and chemical perturbations. (A) UMAP visualization of Perturbverse embeddings for all perturbations across A549, VCAP, and HT29 cell lines. **(B)** Radar plots comparing the cosine similarity between X-Pert–prioritized drugs and randomly selected drugs. Cosine similarity was calculated between the prioritized compounds and ground-truth drugs known to interact with the corresponding genes, as obtained from the DGIdb database. Lines denote the mean values, and shaded areas denote standard deviations across samples. **(C)** UMAP visualization of held-out test perturbations in the HT29 cell line, with the two highlighted subgroups shown with their corresponding perturbation names. Black lines denote biologically plausible relationships. **(D)** Histogram showing the distribution of cosine similarities between 1,919 natural compounds from the SelleckChem database and the BRAF perturbation embedding in the Perturbverse space. (E) Top ten drugs with the highest similarities with BRAF perturbation, shown with their rankings and compound names.

Discussion

In this study, we introduced X-Pert, a unified framework that not only achieves accurate prediction across genetic and chemical perturbations, but also constructs a shared perturbation embedding space, the Perturbverse, that supports systematic interpretation and exploration of perturbation effects. The strong performance and wide-ranging capability arise from its architectural design. By combining a Perturbation Perceiver with a transformer-based Cell Encoder, X-Pert explicitly models fine-grained gene–perturbation interactions while maintaining the intrinsic structure of cell states. This design results in strong performance across tasks ranging from unseen perturbation prediction to combinatorial and dose/efficacy-aware modeling. Beyond predictive accuracy, the Perturbverse provides an interpretable latent space in which different types of perturbations can be compared, aligned, and retrieved, opening new possibilities for drug discovery and gene–

drug association investigation.

Although our work primarily focused on genetic and chemical perturbations, the design of X-Pert renders it inherently extensible to additional perturbation types. Furthermore, the transformer-based architecture and the design of Perturbation Perceiver make X-Pert naturally suited for pre-training on large-scale perturbation corpora. As single-cell perturbation technologies continue to mature, the volume of such datasets will create opportunities to establish X-Pert as a foundation model for perturbation biology, capable of integrating heterogeneous data across platforms, cell types, and perturbation types.

Most existing computational approaches to perturbation modeling have focused almost exclusively on RNA transcriptomic profiles[17-22], reflecting the widespread adoption of single-cell RNA sequencing (scRNA-seq) as the most mature and accessible technology for large-scale single-cell profiling. However, advances in sequencing and profiling technologies are rapidly expanding the omics modalities available for perturbation studies, including epigenomic readouts[88] and protein expression measurements[89] at single-cell resolution. These developments call for methods that can move beyond RNA-centric prediction to jointly capture multi-modal perturbation effects, encompassing RNA, DNA regulatory features, and protein-level responses. The growing availability of such datasets also opens avenues for the development of foundation models, capable of learning universal representations that generalize across biological contexts[90, 91]. In this work, we adopted a scRNA-seq foundation model[20] as the backbone of X-Pert, and X-Pert's modular design makes it readily extensible to additional omics layers, positioning it as a candidate perturbation foundation model that integrates transcriptomic, epigenomic, and proteomic data to capture the full spectrum of cellular responses to external perturbations.

A central challenge in advancing perturbation modeling lies in defining what it truly means for a model to be "accurate". Conventional evaluation metrics, such as correlation across genes, often overestimate performance by rewarding the recovery of shared expression patterns rather than the reconstruction of causal, perturbation-specific effects. This issue extends beyond benchmarking, because it fundamentally shapes how models are trained and optimized. Our work emphasizes that evaluating predictive accuracy from the perspective of biological function is crucial for capturing genuine regulatory responses, as it reflects how well a model understands cellular mechanisms rather than statistical associations. Nevertheless, the metrics proposed in this study represent only an initial step toward evaluating *in silico* perturbation models from a biological perspective. Future progress will depend on developing a broader suite of complementary metrics that can more effectively disentangle true causal perturbation responses from confounding factors and technical artifacts.

Another critical direction concerns data: generating large-scale perturbation corpora while addressing intrinsic challenges such as batch effects, cellular heterogeneity, and stochasticity. Although our study paired original and perturbed cells, we recognize that cells are inherently dynamic and noisy, and it remains difficult to disentangle true signals from background variation. By building on the foundation provided by X-Pert's

framework, future efforts can expand toward a true perturbation foundation model and ultimately a virtual cell, offering unprecedented power for understanding and engineering cellular responses.

Methods

Perturbation Perceiver

Perturbation Resampler

The Perturbation Perceiver, inspired by the perceiver architecture used in image–text multi-modal models[92], is designed to integrate heterogeneous perturbations into a unified latent representation. Formally, let $\boldsymbol{X}_p \in \mathbb{R}^{n_p \times d}$ denote the perturbation embeddings, where n_p is the number of perturbation tokens and d is the latent dimensionality. We additionally introduce a set of learnable latent queries $\boldsymbol{X}_l \in \mathbb{R}^{n_l \times d}$, where n_l is fixed and independent of the type or number of perturbations. In the attention layer, the latent queries are used to extract information from both the perturbation inputs and the latent space itself. Specifically, the queries are defined as $\boldsymbol{Q} = \boldsymbol{X}_l$, while the keys and values are constructed by concatenating the perturbation embeddings with the latent queries: $\boldsymbol{K} = \boldsymbol{V} = [\boldsymbol{X}_p, \boldsymbol{X}_l]$. The attention operation is then given by

$$\mathrm{Attn}(\boldsymbol{Q}, \boldsymbol{K}, \boldsymbol{V}) = \mathrm{softmax}\left(\frac{\boldsymbol{Q}\boldsymbol{K}^{\mathrm{T}}}{\sqrt{d}}\right)\boldsymbol{V}.$$

The output of the attention block is subsequently passed through a feed-forward network (FFN) with residual connections to enhance representational capacity and stabilize training:

$$h = \mathrm{FFN}(\mathrm{Attn}(\boldsymbol{Q}, \boldsymbol{K}, \boldsymbol{V}) + \boldsymbol{X}_l) + \boldsymbol{X}_l.$$

We set the number of latent queries $n_l = 12$ and embedding dimension $d = 512$. The Perturbation Perceiver consists of 2 attention layers, each employing a multi-head attention mechanism with 8 heads. The final output of Perturbation Perceiver is denoted as $\boldsymbol{X} \in \mathbb{R}^{n_l \times d}$, which serves as the keys and values for the downstream Cell Encoder. This design enables Perturbation Perceiver to project perturbations of diverse types into a shared latent space, providing a unified and flexible representation that can be seamlessly integrated by the Cell Encoder for subsequent modeling of perturbation–gene interactions.

Perturbation-type–specific encoders

For different perturbation types, we employ type-specific encoders to transform the raw perturbation embeddings into the input space of the Perturbation Resampler. Specifically, for genetic perturbations we denote the original input as $\boldsymbol{X}_p^g = [\boldsymbol{x}_1^g, \dots, \boldsymbol{x}_{n_p}^g]$, and for chemical perturbations we denote the input as $\boldsymbol{X}_p^m = [\boldsymbol{x}_1^m, \dots, \boldsymbol{x}_{n_p}^m]$, where $\boldsymbol{x}_i^g$ and $\boldsymbol{x}_i^m$ represent individual genetic and chemical perturbation embeddings,

respectively. To ensure that perturbations of different types are mapped into a comparable latent space, we use separate three-layer multilayer perceptrons (MLPs) to project the original embeddings:

$$\boldsymbol{X}_p = \widehat{\boldsymbol{X}}_p^g = f_g(\boldsymbol{X}_p^g), \qquad \boldsymbol{X}_p = \widehat{\boldsymbol{X}}_p^m = f_m(\boldsymbol{X}_p^m),$$

where $f_g(\cdot)$ and $f_m(\cdot)$ denote the genetic and chemical encoders, respectively. These MLP-based encoders enable flexible handling of heterogeneous perturbation types while maintaining a unified representation that can be processed by the Perturbation Resampler.

For genetic perturbations, we leverage large language models (LLMs) to generate raw perturbation embeddings, motivated by the fact that LLMs capture broad biological knowledge across genes through large-scale pretraining. For each target gene, we constructed a natural language prompt of the form: "Impact of knocking out the gene {gene_name} on cell phenotype?" and submitted it to the GPT-4o model. The generated textual response, which encodes functional information about the gene perturbation, was then transformed into a numerical embedding using the GPT text-embedding-ada-002 model, resulting in a 1536-dimensional vector that serves as the raw genetic perturbation embedding.

For chemical perturbations, we adopted a cheminformatics-based approach. Each molecule was represented by its SMILES string, and the RDKit library[33] was used to compute chemical embeddings via Morgan fingerprints. This procedure generated 1024-dimensional binary vectors, where each dimension (0/1) indicates the presence or absence of a specific chemical substructure feature.

Finally, to map perturbations from both types into a shared latent space, the perturbation-type–specific projection networks $f_g(\cdot)$ and $f_m(\cdot)$, were applied. These networks reduce the dimensionality of the raw embeddings from 1536 (genes) and 1024 (molecules) down to a unified 512-dimensional representation, which serves as the input for the Perturbation Resampler.

Perturbation strength incorporation

The perturbation strength (dose or efficacy) can also be incorporated into the Perturbation Perceiver framework, encompassing both the dose information for chemical perturbations and the efficacy information for genetic perturbations. Formally, for input perturbation embeddings $\boldsymbol{X}_p = [\boldsymbol{x}_1, \dots, \boldsymbol{x}_{n_p}]$, we denote the strength for each perturbation $\boldsymbol{x}_i$ as $s_i \in \mathbb{R}$. To integrate this factor, we introduce a learnable vector $\boldsymbol{w} \in \mathbb{R}^d$ that modulates the embedding dimensions according to the perturbation strength. When strength information is included, the original perturbation embedding is modified as:

$$\tilde{\boldsymbol{x}}_i = \boldsymbol{x}_i \odot (s_i \cdot \boldsymbol{w}),$$

where $\odot$ denotes element-wise multiplication. This formulation allows the perturbation embedding to be adaptively scaled according to its strength.

For genetic perturbations, the perturbation strength is equivalent to perturbation efficacy, which we estimate

by comparing gene expression levels between original and perturbed cells. Let μ_c denote the average expression level of the target gene in original cells, and μ_p denote its expression level in perturbed cells. The perturbation efficacy is then defined as:

$$s_i = \frac{\mu_p - \mu_c}{\mu_c}.$$

An efficacy value of −1 corresponds to complete knockout, meaning the target gene is reduced to zero expression relative to original cells.

For chemical perturbations, strength information is typically encoded as dose. For instance, in the Sciplex-3 dataset, each molecule is profiled under four concentrations: 10 nM, 100 nM, 1,000 nM, and 10,000 nM. We apply a $\log_{10}$ transformation to normalize the dose levels, yielding dose-based strength values that are more consistent for model integration: $s_i = \log_{10} \text{dose}$.

In this way, the Perturbation Perceiver framework can incorporate quantitative measures of perturbation strength across types, providing a more nuanced and biologically informed representation of perturbations.

Cell Encoder

Original cell input modelling

In the Cell Encoder, the input original cell is represented with three types of tokens: identity tokens, value tokens, and impact tokens. Following the design philosophy of previous single-cell foundation models, we treat the gene expression profile of a cell analogously to a sentence, where each gene corresponds to a word. Identity tokens are defined as gene identifiers, and we adopt the vocabulary from scGPT[20] to represent them as the scGPT model supports efficient training. For genes not present in the original vocabulary, we extend the vocabulary by adding the new gene identifiers and initialize their embeddings using a uniform distribution matched to the mean and variance of the pretrained gene embeddings. For a given cell, the identity token sequence is thus represented as:

$$\boldsymbol{g} = [\mathrm{id}(g_1), \mathrm{id}(g_2), \dots, \mathrm{id}(g_m)],$$

where $\mathrm{id}(g_i)$ denotes the index of g_i in the vocabulary and m is the total number of genes.

The value tokens represent the expression levels of the corresponding genes and are denoted as

$$\boldsymbol{v} = [v_1, v_2, \dots, v_m],$$

where v_i is typically the log-normalized expression value of gene i.

The impact tokens are designed to capture perturbation–gene interactions and vary depending on the perturbation type. For genetic perturbations, they are defined as

$$\boldsymbol{p} = \boldsymbol{p}_g = [p_1, p_2, \dots, p_m],$$

$$p_i = \begin{cases} 1, \text{if gene } i \text{ is perturbed} \\ 0, \text{else} \end{cases}$$

For chemical perturbations, they are defined as

$$\boldsymbol{p} = \boldsymbol{p}_m = [p_1, p_2, \dots, p_m],$$

where p_i represents the affinity score between the protein encoded by gene i and the input molecule, calculated by inputting the protein sequence and the chemical SMILES string into a pretrained GraphDTA model.

The final embedding for an original cell is then obtained by summing the three projected components:

$$\boldsymbol{h} = \text{embed}_{\text{id}}(\boldsymbol{g}) + \text{embed}_{\text{value}}(\boldsymbol{v}) + \text{embed}_{\text{impact}}(\boldsymbol{p}),$$

where $\text{embed}_{\text{id}}(\cdot)$ projects gene identifiers into embeddings, $\text{embed}_{\text{value}}(\cdot)$ is a nonlinear neural network mapping continuous expression values into embeddings, and $\text{embed}_{\text{impact}}(\cdot)$ projects either binary perturbation indicators or affinity scores into embeddings depending on the perturbation type. All embedding dimensions are set to 512, consistent with the Perturbation Perceiver.

Transformer layers

The transformer layers in the Cell Encoder are designed to integrate the original cell input with perturbation information. Each layer is composed of two modules: a gated cross-attention layer that incorporates perturbation signals into the gene-expression representation, and a self-attention layer that models dependencies among genes.

In the gated cross-attention layer, cross-attention is performed between gene-expression tokens and perturbation embeddings, with an additional gating mechanism that adaptively regulates the strength of perturbation influence. Formally, given the perturbation embeddings $\boldsymbol{X}$ and the l-th layer output of gene-expression tokens $\boldsymbol{H}^{(l)} \in \mathbb{R}^{m \times d}$, the cross-attention is defined as:

$$\boldsymbol{Q}_c = \boldsymbol{H}^{(l)} \boldsymbol{W}_Q^c, \boldsymbol{K}_c = \boldsymbol{X} \boldsymbol{W}_Q^c, \boldsymbol{V}_c = \boldsymbol{X} \boldsymbol{W}_V^c,$$

$$\boldsymbol{C} = \text{softmax}\left(\frac{\boldsymbol{Q}_c \boldsymbol{K}_c^T}{\sqrt{d}}\right) \boldsymbol{V}_c.$$

The gating mechanism is then applied to adaptively regulate the perturbation contribution:

$$\widetilde{\boldsymbol{H}} = \text{LN}\left(\boldsymbol{H}^{(l)} + \tanh\left(\boldsymbol{H}^{(l)} \boldsymbol{W}_{g1} + \boldsymbol{b}_{g1}\right) \odot \boldsymbol{C}\right),$$

where $\text{LN}(\cdot)$ denotes layer normalization. The gated features are further refined with a gated feed-forward network:

$$\boldsymbol{H}_c = \mathrm{LN}\left(\widetilde{\boldsymbol{H}} + \tanh\left(\widetilde{\boldsymbol{H}}\boldsymbol{W}_{g2} + \boldsymbol{b}_{g2}\right) \odot \mathrm{FFN}\left(\widetilde{\boldsymbol{H}}\right)\right).$$

The output $\boldsymbol{H}_c$ is then passed through a standard Transformer encoder block to capture gene–gene dependencies. Multi-head self-attention is applied as:

$$\boldsymbol{Q} = \boldsymbol{H}_c\boldsymbol{W}_Q, \boldsymbol{K} = \boldsymbol{H}_c\boldsymbol{W}_K, \boldsymbol{V} = \boldsymbol{H}_c\boldsymbol{W}_V,$$

$$\boldsymbol{S} = \mathrm{softmax}\left(\frac{\boldsymbol{Q}\boldsymbol{K}^{\mathrm{T}}}{\sqrt{d_k}}\right)\boldsymbol{V}.$$

Residual connections and a feed-forward layer are applied to update the representation:

$$\widehat{\boldsymbol{H}} = \mathrm{LN}(\boldsymbol{H}_c + \boldsymbol{S}),$$

$$\boldsymbol{H}^{(l+1)} = \mathrm{LN}\left(\widehat{\boldsymbol{H}} + \mathrm{FFN}\left(\widehat{\boldsymbol{H}}\right)\right).$$

All $\boldsymbol{W}_*$ and $\boldsymbol{b}_*$ are trainable parameters. In summary, the entire encoder layer alternates between gated cross-attention and self-attention modules:

$$\boldsymbol{H} = \boldsymbol{H}^{(0)},$$

$$\boldsymbol{H}^{(l+1)} = \mathrm{SelfAttnBlock}\left(\mathrm{CrossAttnBlock}\left(\boldsymbol{H}^{(l)}\right)\right), \forall l \in [0, n_l - 1].$$

In this study, we set the number of encoder layers to $n_l = 12$, with 8 attention heads in each multi-head attention module.

Gene expression value decoder

The final output of the transformer layers is passed to the gene expression decoder, which predicts the complete gene expression profile of the perturbed cell. Let the output of the last transformer layer be denoted as $\boldsymbol{H}^{(n_l)} = [\boldsymbol{h}_1^{(n_l)}, \boldsymbol{h}_2^{(n_l)}, \dots, \boldsymbol{h}_m^{(n_l)}]$, where $\boldsymbol{h}_i^{(n_l)}$ represents the latent embedding corresponding to gene i, and m is the total number of genes. For each output token, the decoder projects the latent representation into a scalar expression value:

$$\hat{y}_i = f_d\left(\boldsymbol{h}_i^{(n_l)}\right),$$

where $f_d(\cdot)$ is a nonlinear projection layer implemented as a neural network.

Model training is performed by minimizing the mean squared error (MSE) loss between predicted and ground-truth perturbed expression values:

$$\mathcal{L}_{\mathrm{MSE}} = \frac{1}{m}\sum_{i=1}^{m}(y_i - \hat{y}_i)^2,$$

where y_i denotes the experimentally measured expression level of gene i under perturbation, and $\hat{y}_i$ is the

corresponding model prediction. This objective directly enforces accurate reconstruction of perturbation-induced transcriptional responses at the genome-wide level.

Co-training across different perturbation types

For the X-Pert model trained jointly on genetic and chemical perturbations, we denote k as the total number of samples in a mini-batch, with k_g and k_m representing the number of genetic and chemical perturbation samples, respectively. To encourage alignment between perturbation types, we incorporate a Maximum Mean Discrepancy (MMD) loss that minimizes the distributional gap between the latent embeddings of gene perturbations and drug perturbations. The MMD loss is applied on the outputs of the perturbation-type–specific encoders, thereby enforcing the latent space to capture perturbation representations in a type-agnostic manner.

Formally, the MMD loss is defined as the squared distance between the kernel mean embeddings of the two distributions in a reproducing kernel Hilbert space (RKHS):

$$\mathcal{L}_{\mathrm{MMD}}(\widehat{\boldsymbol{X}}_p^g, \widehat{\boldsymbol{X}}_p^m) = \frac{1}{k_g(k_g-1)}\sum_{i\neq i'} f_k(\boldsymbol{x}_i^g, \boldsymbol{x}_{i'}^g) + \frac{1}{k_m(k_m-1)}\sum_{i\neq i'} f_k(\boldsymbol{x}_i^m, \boldsymbol{x}_{i'}^m) - \frac{2}{k_g k_m}\sum_{i=1}^{k_g}\sum_{j=1}^{k_m} f_k(\boldsymbol{x}_i^g, \boldsymbol{x}_j^m),$$

where $\mathrm{f_k}(\cdot,\cdot)$ is the kernel function. We adopt the radial basis function (RBF) kernel, also known as the Gaussian kernel, defined as:

$$f_k(\boldsymbol{x}, \boldsymbol{y}) = \exp\left(-\frac{||\boldsymbol{x}-\boldsymbol{y}||^2}{2\sigma^2}\right),$$

where $||\boldsymbol{x}-\boldsymbol{y}||^2$ denotes the squared Euclidean distance between vectors $\boldsymbol{x}$ and $\boldsymbol{y}$, and $\sigma > 0$ is the kernel bandwidth controlling the smoothness of the similarity measure. Following common practice, we set σ using the median heuristic, which has been shown to yield stable performance in high-dimensional spaces.

The overall training objective combines the MSE loss with the alignment loss:

$$\mathcal{L}_{\mathrm{total}} = \mathcal{L}_{\mathrm{MSE}} + \alpha\mathcal{L}_{\mathrm{MMD}},$$

where α is a balancing hyperparameter. In this study, we set $\alpha = 0.2$, which we found to provide a good trade-off between accurate reconstruction and effective cross–perturbation-type alignment.

Perturbverse embedding extraction

We use the output of the Perturbation Perceiver, $\boldsymbol{X} \in \mathbb{R}^{n_l \times d}$, as the Perturbverse representation of the input perturbations. Since the number of latent queries n_l is fixed at 12, this design ensures that perturbations of

any type, regardless of their original perturbation type or number of input tokens, are consistently projected into a standardized latent space of dimension 12×512. To obtain a compact perturbation embedding, the latent tokens are subsequently flattened into a 6,144-dimensional vector, which serves as the unified latent representation of the perturbation.

Model evaluation

We used several metrics to perform the model evaluation and application.

Pearson correlation coefficient (PCC)

The PCC measures the linear correlation between predicted $(\hat{y})$ and observed (y) values:

$$\mathrm{PCC}(y,\hat{y}) = \frac{\sum_{i=1}^{m}(y_i - \bar{y})(\hat{y}_i - \bar{\hat{y}})}{\sqrt{\sum_{i=1}^{m}(y_i - \bar{y})^2}\sqrt{\sum_{i=1}^{m}(\hat{y}_i - \bar{\hat{y}})^2}},$$

where $\bar{y}$ and $\bar{\hat{y}}$ denote the means of the true and predicted values, respectively.

Coefficient of determination (R^2)

The R^2 score quantifies the proportion of variance in the observed data explained by the predictions:

$$R^2(y,\hat{y}) = 1 - \frac{\sum_{i=1}^{m}(y_i - \hat{y}_i)^2}{\sum_{i=1}^{m}(y_i - \bar{y})^2}.$$

Higher values indicate stronger predictive power, with $R^2 = 1$ representing perfect prediction.

Energy distance (E-distance)

The E-distance evaluates the dissimilarity between the distributions of perturbed and original cells, serving as a measure of perturbation effect size. Given two sets of samples $\boldsymbol{X} = \{\boldsymbol{x}_1, \dots, \boldsymbol{x}_n\}$ and $\boldsymbol{Y} = \{\boldsymbol{y}_1, \dots, \boldsymbol{y}_m\}$, the E-distance is defined as:

$$\mathrm{E}(\boldsymbol{X},\boldsymbol{Y}) = \frac{2}{nm}\sum_{i=1}^{n}\sum_{j=1}^{m}||\boldsymbol{x}_i - \boldsymbol{y}_j|| - \frac{1}{n^2}\sum_{i=1}^{n}\sum_{j=1}^{m}||\boldsymbol{x}_i - \boldsymbol{x}_j|| - \frac{1}{m^2}\sum_{i=1}^{n}\sum_{j=1}^{m}||\boldsymbol{y}_i - \boldsymbol{y}_j||.$$

We use the scPerturb package to calculate the E-distance.

Cosine similarity

Cosine similarity measures the angle between two vectors and evaluates their directional similarity:

$$\mathrm{CosSim}(y, \hat{y}) = \frac{\sum_{i=1}^{m} y_i \, \hat{y}_i}{\sqrt{\sum_{i=1}^{m} y_i^2} \sqrt{\sum_{i=1}^{m} \hat{y}_i^2}}.$$

This metric is scale-invariant and emphasizes relative patterns rather than absolute magnitude.

Perturbation quantification with Hallmark gene sets

For each genetic perturbation, we evaluated pathway-level transcriptional changes by calculating gene set scores across all single cells. We used the Hallmark gene sets[40] from the Molecular Signatures Database (MSigDB), which consist of 50 curated collections that capture and summarize specific, well-defined biological processes and cell states. These gene sets provide a compact and biologically interpretable representation of transcriptional programs, allowing us to assess whether perturbations induce consistent pathway-level responses. Gene set scores were computed using the Scanpy package[93], specifically the 'sc.tl.score_genes' function, which calculates a per-cell enrichment score by comparing the expression of genes within each gene set against a reference background.

KNN accuracy

To quantitatively assess the discriminative ability of the learned Perturbverse embeddings (Fig. S2A), we employed a *K*-nearest neighbor (KNN) classification framework with stratified five-fold cross-validation. Specifically, a KNN classifier ($K = 5$) was trained on the PCA-transformed feature space, and the resulting predictions were evaluated using confusion matrices aggregated across folds. For each class (corresponding to a pathway label), a per-class accuracy was computed as the ratio of correctly classified samples to the total number of true samples in that class. This metric provides a fine-grained evaluation of how well the embedding preserves class-specific separability, independent of class imbalance.

Databases and datasets

Candidate drug databases

We employed three different drug databases as candidate libraries to support perturbation retrieval and *in silico* drug screening tasks. For the drug perturbation retrieval experiment (Fig. 4G), we used the HERB 2.0 database[46], which contains 30,916 natural compounds with curated annotations of chemical structures and pharmacological information. For the *in silico* drug screening task (Fig. 5D), we used an FDA-approved drug library from TargetMol[94], consisting of 935 clinically approved compounds, ensuring the relevance of predictions to translational applications. Finally, for the cross-type perturbation retrieval analysis (Fig. 6E), we utilized a unique collection of 1,930 monomeric compounds derived from traditional Chinese medicine (TCM) curated by SelleckChem[83], which provides structurally diverse natural products not typically represented in standard drug libraries.

730 **Genetic and chemical perturbation data**

731 We benchmarked X-Pert against multiple competing methods on genetic perturbation prediction using four
732 datasets: Replogle2022_K562[4], Replogle2022_RPE1[4], and Norman2019[35]. The raw data of all the datasets
733 were obtained from the scPerturb[16] database.

734 For chemical perturbation benchmarking, we employed the Sciplex-3[11] and CMAP[44] datasets. The Sciplex-
735 3 dataset is a single-cell perturbation dataset comprising 758,360 processed cells across three cell lines and
736 188 small-molecule perturbations after preprocessing. The CMAP dataset, which provides bulk-level gene
737 expression profiles, contains 678,401 samples spanning 70 cell lines and 17,775 chemical perturbations after
738 preprocessing.

739 All the datasets are processed with the same procedure following our previous benchmark[38]:

740 - Feature Selection: Top 5,000 highly variable genes (HVGs) were identified from each dataset using
741 standard procedures. We also included all perturbed genes originally present in the dataset's feature list.

742 - Normalization: Raw count data was normalized using the log-normalization method, implemented
743 through the standard preprocessing workflow of Scanpy[93].

744 - Original-cell pairing: For every cell subjected to perturbation, we randomly sampled an original cell from
745 the same dataset to form a pre- and post-perturbation cell pair. These pairs served as the basis for training
746 and evaluating models.

747 - Identifying differentially expressed genes (DEGs): For each perturbation, we identified DEGs by
748 comparing perturbed cells to original cells. Genes were ranked based on adjusted *p*-values computed
749 using the Wilcoxon test in Scanpy, with those having adjusted *p*-values < 0.05 designated as DEGs.

750 **Tahoe-100M**

751 Tahoe-100M is an exceptionally large-scale chemical perturbation dataset comprising approximately one
752 million single cells. To reduce data redundancy and facilitate efficient training, we aggregated single-cell
753 profiles into pseudo-bulk samples: for each combination for drug, cell line, and dose, the expression values of
754 all corresponding single cells were averaged to yield a representative profile. After this preprocessing step, a
755 total of 65,768 pseudo-bulk samples were retained for model training. To ensure that the model focuses on
756 biologically informative signals, we further selected 10,000 highly variable genes (HVGs) across all samples
757 as the feature set. This dimensionality reduction strategy retains the genes with the largest expression
758 variability, thereby capturing the most relevant transcriptional changes induced by perturbations while
759 reducing noise from less informative features.

760

761 ***In silico* drug screening with X-Pert**

To perform *in silico* drug screening, we combined disease-associated gene signatures with X-Pert–predicted gene expression profiles under drug perturbations. Disease signatures were obtained from the CRowd Extracted Expression of Differential Signatures (CREEDS) database[95], which contains 839 annotated disease-versus-normal transcriptional signatures. For each disease, CREEDS provides two complementary gene sets: one consisting of up-regulated genes associated with the disease state, and another consisting of down-regulated genes. The rationale of our approach is that a drug with therapeutic potential should simultaneously suppress the disease-associated up-regulated genes while inducing the disease-associated down-regulated genes, thereby reversing the pathological transcriptional program.

We applied this framework to cell lines with defined disease associations in Tahoe-100M. For example, in the HepG2 cell line (originating from hepatocellular carcinoma, HCC), we used X-Pert to predict transcriptional responses to 831 candidate drugs across the 10,000 highly variable genes selected from the dataset. This produced drug-specific predicted gene expression profiles for HepG2 cells. The corresponding HCC gene signatures from CREEDS were then used to evaluate these predictions. Specifically, we computed two complementary enrichment scores using the Scanpy function 'sc.tl.score_genes': the up-regulated gene set score (up-score) and the down-regulated gene set score (down-score). Intuitively, lower up-scores and higher down-scores represent drugs with higher potential that could reverse disease signatures.

Large-scale chemical perturbation datasets such as Tahoe-100M are subject to technical batch effects, which in this case primarily arise from sequencing plate variability (Fig. 5B). These batch effects introduce systematic biases into X-Pert's predictions, leading to spurious correlations between the calculated up-scores and down-scores. As a result, high up-scores often co-occur with proportionally high down-scores (Fig. 5D). This phenomenon is likely attributable to plate-specific biases in total transcript counts across different drug conditions, which can confound the biological signal and distort the prioritization of candidate drugs.

To mitigate these effects, we implemented a simple yet effective correction strategy based on linear regression. Specifically, we fit a regression line between the up-scores and down-scores across all candidate drugs for a given disease. The fitted line captures the dominant technical trend introduced by batch effects. We then identify drugs with the largest positive residuals (intercepts above the fitted line) as top candidates, since these drugs deviate most strongly from the batch-driven correlation and therefore likely reflect genuine biological activity rather than technical artifacts.

Drugs achieving large positive residuals (simultaneously low up-scores and high down-scores) are prioritized as candidate therapeutic compounds for the corresponding disease. This strategy allows us to systematically evaluate the potential of existing drugs to reverse disease-specific transcriptional dysregulation and highlights X-Pert's utility in drug repurposing.

GDIdb drugs filtering

For the cross-type perturbation retrieval evaluation, we selected drugs known to interact with eight representative genes—AKT1, AKT2, CTSK, SMAD3, TP53, MTOR, BRAF, and PIK3CA—as the ground-truth references. For each gene, we obtained its interacting drugs from the DGIdb database[66], which provides curated drug–gene interactions along with an interaction score that quantifies the strength of evidence supporting each relationship. To ensure reliability, we applied a threshold of 0.2 on the interaction score and retained only those drug–gene pairs exceeding this cutoff. After filtering, the number of drugs associated with each gene ranged from 7 to 23, forming the reference sets for evaluation.

Data availability

The genetic perturbation data (Replogle2022_K562, Replogle2022_RPE1, and Norman2019) were downloaded from https://zenodo.org/records/10044268. The Sciplex-3 data were accessed from https://figshare.com/articles/dataset/sciplex3/22122701. The CMAP data was downloaded from Gene Expression Omnibus (GEO) with accession number GSE92742. The Tahoe-100M data were downloaded from https://huggingface.co/datasets/tahoebio/Tahoe-100M.

Code availability

The code and documents of X-Pert are available at https://github.com/Chen-Li-17/X-Pert.

Acknowledgements

The work is sponsored by The National Key R&D Program of China (2025YFC3409300), National Natural Science Foundation of China (62373210, 62433001, 92470105), and Tsinghua-Toyota Joint Research Institute Inter-Disciplinary Program (20243930093).

Author contributions

C.L., L.W. and X.Z. conceived and designed the study. X.Z and L.W. supervised the study and provided critical revisions. C.L. collected the data, build the model, conducted the experiments, and analyzed the results. C.L. and L.W. drafted the manuscript and prepared the figures. X.Z. reviewed the manuscript and provided critical insights. All authors contributed to reviewing and approving the final manuscript.

Competing interests

826 The authors declare no competing interests.

Reference

1. Dixit, A. et al. Perturb-Seq: Dissecting Molecular Circuits with Scalable Single-Cell RNA Profiling of Pooled Genetic Screens. *Cell* **167**, 1853-1866 e1817 (2016).

2. Adamson, B. et al. A Multiplexed Single-Cell CRISPR Screening Platform Enables Systematic Dissection of the Unfolded Protein Response. *Cell* **167**, 1867-1882 e1821 (2016).

3. Datlinger, P. et al. Pooled CRISPR screening with single-cell transcriptome readout. *Nat Methods* **14**, 297-301 (2017).

4. Replogle, J.M. et al. Mapping information-rich genotype-phenotype landscapes with genome-scale Perturb-seq. *Cell* **185**, 2559-2575 e2528 (2022).

5. Rubin, A.J. et al. Coupled Single-Cell CRISPR Screening and Epigenomic Profiling Reveals Causal Gene Regulatory Networks. *Cell* **176**, 361-376 e317 (2019).

6. Wessels, H.H. et al. Efficient combinatorial targeting of RNA transcripts in single cells with Cas13 RNA Perturb-seq. *Nat Methods* **20**, 86-94 (2023).

7. Otto, J.E. et al. Structural and functional properties of mSWI/SNF chromatin remodeling complexes revealed through single-cell perturbation screens. *Mol Cell* **83**, 1350-1367 e1357 (2023).

8. Aissa, A.F. et al. Single-cell transcriptional changes associated with drug tolerance and response to combination therapies in cancer. *Nat Commun* **12**, 1628 (2021).

9. Chang, M.T. et al. Identifying transcriptional programs underlying cancer drug response with TraCe-seq. *Nat Biotechnol* **40**, 86-93 (2022).

10. Zhao, W. et al. Deconvolution of cell type-specific drug responses in human tumor tissue with single-cell RNA-seq. *Genome Med* **13**, 82 (2021).

11. Srivatsan, S.R. et al. Massively multiplex chemical transcriptomics at single-cell resolution. *Science* **367**, 45-51 (2020).

12. Zhang, J. et al. Tahoe-100m: A giga-scale single-cell perturbation atlas for context-dependent gene function and cellular modeling. *bioRxiv*, https://doi.org/10.1101/2025.1102.1120.639398 (2025).

13. Papalexi, E. et al. Characterizing the molecular regulation of inhibitory immune checkpoints with multimodal single-cell screens. *Nat Genet* **53**, 322-331 (2021).

14. Frangieh, C.J. et al. Multimodal pooled Perturb-CITE-seq screens in patient models define mechanisms of cancer immune evasion. *Nat Genet* **53**, 332-341 (2021).

15. Yang, B. et al. PerturbDB for unraveling gene functions and regulatory networks. *Nucleic Acids Res* **53**, D1120-D1131 (2025).

16. Peidli, S. et al. scPerturb: harmonized single-cell perturbation data. *Nat Methods* **21**, 531-540 (2024).

17. Roohani, Y., Huang, K. & Leskovec, J. Predicting transcriptional outcomes of novel multigene perturbations with GEARS. *Nat Biotechnol* **42**, 927-935 (2024).

18. Bai, D., Ellington, C.N., Mo, S., Song, L. & Xing, E.P. AttentionPert: accurately modeling multiplexed genetic perturbations with multi-scale effects. *Bioinformatics* **40**, i453-i461 (2024).

19. Hao, M. et al. Large-scale foundation model on single-cell transcriptomics. *Nat Methods* **21**,

1481-1491 (2024).

20. Cui, H. et al. scGPT: toward building a foundation model for single-cell multi-omics using generative AI. *Nat Methods* **21**, 1470-1480 (2024).

21. Schrod, S., Zacharias, H.U., Beissbarth, T., Hauschild, A.C. & Altenbuchinger, M. CODEX: COunterfactual Deep learning for the in silico EXploration of cancer cell line perturbations. *Bioinformatics* **40**, i91-i99 (2024).

22. Yu, H., Qian, W., Song, Y. & Welch, J.D. PerturbNet predicts single-cell responses to unseen chemical and genetic perturbations. *Mol Syst Biol* **21**, 960-982 (2025).

23. Xu, Y., Fleming, S., Tegtmeyer, M., McCarroll, S.A. & Babadi, M. Explainable modeling of single-cell perturbation data using attention and sparse dictionary learning. *Cell Syst* **16**, 101245 (2025).

24. Hetzel, L. et al. Predicting Cellular Responses to Novel Drug Perturbations at a Single-Cell Resolution [C]. Proceedings of the 36th Conference on Neural Information Processing Systems (NeurIPS). 2022.

25. Piran, Z., Cohen, N., Hoshen, Y. & Nitzan, M. Disentanglement of single-cell data with biolord. *Nat Biotechnol* **42**, 1678-1683 (2024).

26. Qi, X. et al. Predicting transcriptional responses to novel chemical perturbations using deep generative model for drug discovery. *Nat Commun* **15**, 9256 (2024).

27. Maleki, S. et al. Efficient Fine-Tuning of Single-Cell Foundation Models Enables Zero-Shot Molecular Perturbation Prediction. *arXiv preprint arXiv:2412.13478* (2024).

28. Klein, D. et al. CellFlow enables generative single-cell phenotype modeling with flow matching. *bioRxiv*, https://doi.org/10.1101/2025.1104.1111.648220 (2025).

29. Adduri, A.K. et al. Predicting cellular responses to perturbation across diverse contexts with STATE. *bioRxiv*, https://doi.org/10.1101/2025.1106.1126.661135 (2025).

30. Li, C. et al. TFcomb identifies transcription factor combinations for cellular reprogramming based on single-cell multiomics data. *Genome Res* **35**, 1429-1439 (2025).

31. Cui, A. et al. Dictionary of immune responses to cytokines at single-cell resolution. *Nature* **625**, 377-384 (2024).

32. OpenAI GPT-4 Technical Report. *arXiv:2303.08774* (2023).

33. Bento, A.P. et al. An open source chemical structure curation pipeline using RDKit. *J Cheminform* **12**, 51 (2020).

34. Nguyen, T. et al. GraphDTA: predicting drug-target binding affinity with graph neural networks. *Bioinformatics* **37**, 1140-1147 (2021).

35. Norman, T.M. et al. Exploring genetic interaction manifolds constructed from rich single-cell phenotypes. *Science* **365**, 786-793 (2019).

36. Ahlmann-Eltze, C., Huber, W. & Anders, S.J.N.M. Deep-learning-based gene perturbation effect prediction does not yet outperform simple linear baselines. *Nat Methods*, 1-5 (2025).

37. Kamimoto, K. et al. Dissecting cell identity via network inference and in silico gene perturbation. *Nature* **614**, 742-751 (2023).

38. Li, C. et al. Benchmarking AI models for in silico gene perturbation of cells. *bioRxiv*, https://doi.org/10.1101/2024.1112.1120.629581 (2024).

39. Vinas Torne, R. et al. Systema: a framework for evaluating genetic perturbation response

prediction beyond systematic variation. *Nat Biotechnol* (2025).

40. Liberzon, A. et al. The Molecular Signatures Database (MSigDB) hallmark gene set collection. *Cell Syst* **1**, 417-425 (2015).

41. Radhakrishnan, S.K. et al. Transcription factor Nrf1 mediates the proteasome recovery pathway after proteasome inhibition in mammalian cells. *Mol Cell* **38**, 17-28 (2010).

42. Oron, M. et al. The molecular network of the proteasome machinery inhibition response is orchestrated by HSP70, revealing vulnerabilities in cancer cells. *Cell Rep* **40**, 111428 (2022).

43. Volmar, C.H. et al. M344 promotes nonamyloidogenic amyloid precursor protein processing while normalizing Alzheimer's disease genes and improving memory. *Proc Natl Acad Sci U S A* **114**, E9135-E9144 (2017).

44. Subramanian, A. et al. A Next Generation Connectivity Map: L1000 Platform and the First 1,000,000 Profiles. *Cell* **171**, 1437-1452 e1417 (2017).

45. Knox, C. et al. DrugBank 6.0: the DrugBank Knowledgebase for 2024. *Nucleic Acids Res* **52**, D1265-D1275 (2024).

46. Gao, K. et al. HERB 2.0: an updated database integrating clinical and experimental evidence for traditional Chinese medicine. *Nucleic Acids Res* **53**, D1404-D1414 (2025).

47. Lee, H.K., Oh, S.R., Kim, J.I., Kim, J.W. & Lee, C.O. Agastaquinone, a new cytotoxic diterpenoid quinone from Agastache rugosa. *J Nat Prod* **58**, 1718-1721 (1995).

48. Mosca, L., Ilari, A., Fazi, F., Assaraf, Y.G. & Colotti, G. Taxanes in cancer treatment: Activity, chemoresistance and its overcoming. *Drug Resist Updat* **54**, 100742 (2021).

49. Schneider, F., Samarin, K., Zanella, S. & Gaich, T. Total synthesis of the complex taxane diterpene canataxpropellane. *Science* **367**, 676-681 (2020).

50. Gupta, A., Atanasov, A.G., Li, Y., Kumar, N. & Bishayee, A. Chlorogenic acid for cancer prevention and therapy: Current status on efficacy and mechanisms of action. *Pharmacol Res* **186**, 106505 (2022).

51. Huang, S. et al. Chlorogenic acid effectively treats cancers through induction of cancer cell differentiation. *Theranostics* **9**, 6745-6763 (2019).

52. Ibello, E. et al. Three-dimensional environment sensitizes pancreatic cancer cells to the anti-proliferative effect of budesonide by reprogramming energy metabolism. *J Exp Clin Cancer Res* **43**, 165 (2024).

53. Yalniz, F.F. et al. A phase II study of addition of pracinostat to a hypomethylating agent in patients with myelodysplastic syndromes who have not responded to previous hypomethylating agent therapy. *British journal of haematology* **188**, 404-412 (2020).

54. Sharman, J. et al. An open-label phase 2 trial of entospletinib (GS-9973), a selective spleen tyrosine kinase inhibitor, in chronic lymphocytic leukemia. *Blood* **125**, 2336-2343 (2015).

55. Joshi, S. New insights into SYK targeting in solid tumors. *Trends Pharmacol Sci* **45**, 904-918 (2024).

56. Rohila, D. et al. Syk Inhibition Reprograms Tumor-Associated Macrophages and Overcomes Gemcitabine-Induced Immunosuppression in Pancreatic Ductal Adenocarcinoma. *Cancer Res* **83**, 2675-2689 (2023).

57. Varshosaz, J., Fard, M.M., Mirian, M. & Hassanzadeh, F. Targeted Nanoparticles for Co-delivery of 5-FU and Nitroxoline, a Cathepsin B Inhibitor, in HepG2 Cells of Hepatocellular Carcinoma. *Anticancer Agents Med Chem* **20**, 346-358 (2020).

954 58. Choi, S.M. et al. Clioquinol, a Cu(II)/Zn(II) chelator, inhibits both ubiquitination and
955 asparagine hydroxylation of hypoxia-inducible factor-1alpha, leading to expression of
956 vascular endothelial growth factor and erythropoietin in normoxic cells. *J Biol Chem* **281**,
957 34056-34063 (2006).

958 59. Huang, Z., Wang, L., Chen, L., Zhang, Y. & Shi, P. Induction of cell cycle arrest via the p21,
959 p27-cyclin E,A/Cdk2 pathway in SMMC-7721 hepatoma cells by clioquinol. *Acta Pharm* **65**,
960 463-471 (2015).

961 60. White, J.R., Jr. Empagliflozin, an SGLT2 inhibitor for the treatment of type 2 diabetes
962 mellitus: a review of the evidence. *Ann Pharmacother* **49**, 582-598 (2015).

963 61. Abdelhamid, A.M. et al. Empagliflozin adjunct with metformin for the inhibition of
964 hepatocellular carcinoma progression: Emerging approach for new application. *Biomed*
965 *Pharmacother* **145**, 112455 (2022).

966 62. Scafoglio, C.R. et al. Sodium-glucose transporter 2 is a diagnostic and therapeutic target for
967 early-stage lung adenocarcinoma. *Sci Transl Med* **10** (2018).

968 63. Luo, J., Hendryx, M. & Dong, Y. Sodium-glucose cotransporter 2 (SGLT2) inhibitors and non-
969 small cell lung cancer survival. *Br J Cancer* **128**, 1541-1547 (2023).

970 64. Lu, J. et al. Ciclopirox targets cellular bioenergetics and activates ER stress to induce
971 apoptosis in non-small cell lung cancer cells. *Cell Commun Signal* **20**, 37 (2022).

972 65. Ramalingam, S. et al. A Randomized, Double-Blind, Phase 2 Trial of Veliparib (ABT-888)
973 With Carboplatin and Paclitaxel in Previously Untreated Metastatic or Advanced Non-Small
974 Cell Lung Cancer. *International Journal of Radiation Oncology*Biology*Physics* **90**, S4-S5
975 (2014).

976 66. Cannon, M. et al. DGIdb 5.0: rebuilding the drug-gene interaction database for precision
977 medicine and drug discovery platforms. *Nucleic Acids Res* **52**, D1227-D1235 (2024).

978 67. Dobelis, P., Madl, J.E., Pfister, J.A., Manners, G.D. & Walrond, J.P. Effects of Delphinium
979 alkaloids on neuromuscular transmission. *J Pharmacol Exp Ther* **291**, 538-546 (1999).

980 68. Ahn, E.J. et al. Genotype-Phenotype Correlation of SMN1 and NAIP Deletions in Korean
981 Patients with Spinal Muscular Atrophy. *J Clin Neurol* **13**, 27-31 (2017).

982 69. Lin, J., Wang, Q., Zhou, S., Xu, S. & Yao, K. Tetramethylpyrazine: A review on its
983 mechanisms and functions. *Biomed Pharmacother* **150**, 113005 (2022).

984 70. Xue, Z. et al. MAP3K1 and MAP2K4 mutations are associated with sensitivity to MEK
985 inhibitors in multiple cancer models. *Cell Res* **28**, 719-729 (2018).

986 71. Velasco-Velazquez, M. et al. CCR5 antagonist blocks metastasis of basal breast cancer
987 cells. *Cancer Res* **72**, 3839-3850 (2012).

988 72. Berr, A.L. et al. Vimentin is required for tumor progression and metastasis in a mouse model
989 of non-small cell lung cancer. *Oncogene* **42**, 2074-2087 (2023).

990 73. Perez-Sala, D., Gilbert, B.A., Rando, R.R. & Canada, F.J. Analogs of farnesylcysteine induce
991 apoptosis in HL-60 cells. *FEBS Lett* **426**, 319-324 (1998).

992 74. Huang, S. et al. Ras guanine nucleotide-releasing protein-4 promotes renal inflammatory
993 injury in type 2 diabetes mellitus. *Metabolism* **131**, 155177 (2022).

994 75. Weng, L.Q. et al. Aliskiren ameliorates pressure overload-induced heart hypertrophy and
995 fibrosis in mice. *Acta Pharmacol Sin* **35**, 1005-1014 (2014).

996 76. Zhao, K. et al. Nuclear import of Mas-related G protein-coupled receptor member D induces
997 pathological cardiac remodeling. *Cell Commun Signal* **21**, 181 (2023).

77. Lan, L. et al. Mas-related G protein-coupled receptor D participates in inflammatory pain by promoting NF-kappaB activation through interaction with TAK1 and IKK complex. *Cell Signal* **76**, 109813 (2020).

78. Song, C. et al. Limonin ameliorates dextran sulfate sodium-induced chronic colitis in mice by inhibiting PERK-ATF4-CHOP pathway of ER stress and NF-kappaB signaling. *Int Immunopharmacol* **90**, 107161 (2021).

79. Scheinman, R.I., Gualberto, A., Jewell, C.M., Cidlowski, J.A. & Baldwin, A.S., Jr. Characterization of mechanisms involved in transrepression of NF-kappa B by activated glucocorticoid receptors. *Mol Cell Biol* **15**, 943-953 (1995).

80. Brenachot, X. et al. Hepatic protein tyrosine phosphatase receptor gamma links obesity-induced inflammation to insulin resistance. *Nat Commun* **8**, 1820 (2017).

81. Lin, J., Li, Q., Lei, X. & Zhao, H. The emerging roles of GPR158 in the regulation of the endocrine system. *Front Cell Dev Biol* **10**, 1034348 (2022).

82. Chapdelaine, A.G., Ku, G.C., Sun, G. & Ayrapetov, M.K. The Targeted Degradation of BRAF V600E Reveals the Mechanisms of Resistance to BRAF-Targeted Treatments in Colorectal Cancer Cells. *Cancers (Basel)* **15** (2023).

83. Selleck products. https://www.selleckchem.com/ (2025).

84. Chen, T., Yang, P. & Jia, Y. Molecular mechanisms of astragaloside-IV in cancer therapy (Review). *Int J Mol Med* **47** (2021).

85. Zhang, Y. et al. Glycyrrhetinic acid binds to the conserved P-loop region and interferes with the interaction of RAS-effector proteins. *Acta Pharm Sin B* **9**, 294-303 (2019).

86. Fu, T., Chai, B., Shi, Y., Dang, Y. & Ye, X. Fargesin inhibits melanin synthesis in murine malignant and immortalized melanocytes by regulating PKA/CREB and P38/MAPK signaling pathways. *J Dermatol Sci* **94**, 213-219 (2019).

87. Shi, A., Liu, L., Li, S. & Qi, B. Natural products targeting the MAPK-signaling pathway in cancer: overview. *J Cancer Res Clin Oncol* **150**, 6 (2024).

88. Metzner, E., Southard, K.M. & Norman, T.M. Multiome Perturb-seq unlocks scalable discovery of integrated perturbation effects on the transcriptome and epigenome. *Cell Syst* **16**, 101161 (2025).

89. Saunders, R.A. et al. Perturb-Multimodal: A platform for pooled genetic screens with imaging and sequencing in intact mammalian tissue. *Cell* **188**, 4790-4809 e4722 (2025).

90. Wu, J., Wan, C., Ji, Z., Zhou, Y. & Hou, W. EpiFoundation: A Foundation Model for Single-Cell ATAC-seq via Peak-to-Gene Alignment. *bioRxiv* (2025).

91. Li, W. et al. scPROTEIN: a versatile deep graph contrastive learning framework for single-cell proteomics embedding. *Nat Methods* **21**, 623-634 (2024).

92. Alayrac, J.B. et al. Flamingo: a Visual Language Model for Few-Shot Learning [C]. Proceedings of the 36th Conference on Neural Information Processing Systems (NeurIPS). 2022.

93. Wolf, F.A., Angerer, P. & Theis, F.J. SCANPY: large-scale single-cell gene expression data analysis. *Genome Biol* **19**, 15 (2018).

94. TargetMol. https://www.targetmol.com (2025).

95. Wang, Z. et al. Extraction and analysis of signatures from the Gene Expression Omnibus by the crowd. *Nat Commun* **7**, 12846 (2016).

1041